

## Warm Winter Storms in Central Chile

R. GARREAUD

*Department of Geophysics, and Center for Climate and Resilience Research, University of Chile, Santiago, Chile*

(Manuscript received 10 September 2012, in final form 1 February 2013)

### ABSTRACT

Central Chile is a densely populated region along the west coast of subtropical South America (30°–36°S), limited to the east by the Andes. Precipitation is concentrated in austral winter, mostly associated with the passage of cold fronts. The freezing level over central Chile is typically between 1500 and 2500 m when precipitation is present. In about a third of the cases, however, precipitation occurs accompanied by warm temperatures and freezing levels above 3000 m, leading to a sizeable increment in the pluvial area of Andean basins and setting the stage for hydrometeorological hazards. Here, warm winter storms in central Chile are studied, including a statistical description of their occurrence and an estimate of their hydrological impacts. Remote-sensed data and high-resolution reanalysis are used to explore the synoptic-scale environment of a typical case, generalized later by a compositing analysis. The structure of warm storms is also contrasted with that of the more recurrent cold cases. Precipitation during warm events occurs in the warm sector of a slow-moving cold front because of the intense moisture flux against the mountains in connection with a land-falling atmospheric river. This is in turn driven by a strong zonal jet aloft and reduced mechanical blocking upstream of the Andes. On a broader scale, a key element is the presence of a slowly moving anticyclone over the south Pacific, fostering advection of cold air into midlatitudes. The intense and persistent zonal jet stretches a moist-air corridor from the central Pacific to the west coast of South America.

### 1. Introduction

Central Chile is the narrow (~200 km) strip of land extending from 30° to 36°S along the west coast of South America and limited to the east by the Andes cordillera (Fig. 1). This region hosts more than 8 million inhabitants (about half of the country's population), key economic activities, and major cities, including Santiago (33.5°S), the Chilean capital. Consistent with its location at subtropical latitudes, central Chile is year-round under the influence of the southeast Pacific anticyclone, featuring a semiarid climate between extremely dry conditions to the north and more humid conditions to the south (e.g., Fig. 2b). In the east–west direction, the Andes cordillera—rising over 4000 m MSL—acts as a boundary between the continental climate of central Argentina and the milder, ocean-controlled climate of central Chile (e.g., Garreaud et al. 2009). Annual mean precipitation varies from 200 to 700 mm, depending on latitude and

altitude, and exhibits significant interannual variability associated with the El Niño–Southern Oscillation following a warm–wet cold–dry pattern (Montecinos and Aceituno 2003). Precipitation is largely concentrated in austral winter (May–September) but an important fraction of it is retained as snow over the Andes and subsequently delivered to lowland valleys as meltwater during spring and summer (Cortés et al. 2011) with beneficial effects on agriculture. However, the sharp, complex topography of the Andes, with steep slopes and narrow valleys, also sets the stage for hydrometeorological disasters, including localized flash floods, debris flows, and widespread flooding during wet years (Sepúlveda and Padilla 2008).

The synoptic-scale environment that characterizes central Chile frontal rainstorms has been described in recent works by Falvey and Garreaud (2007), Barrett et al. (2011), and Viale and Nuñez (2011). Between 5 and 15 multiday (1–4) rainfall episodes occur per winter, associated with cold fronts arching equatorward from a surface low moving along the storm track to the south of 40°S (Hoskins and Hodges 2005; see also Catto et al. 2012). Low-level northwesterly flow transports air with high water vapor content from the tropical eastern

---

*Corresponding author address:* Dr. René Garreaud, Department of Geophysics, Universidad de Chile, Blanco Encalada 2002, Santiago, Chile.  
E-mail: rgarreau@dgf.uchile.cl

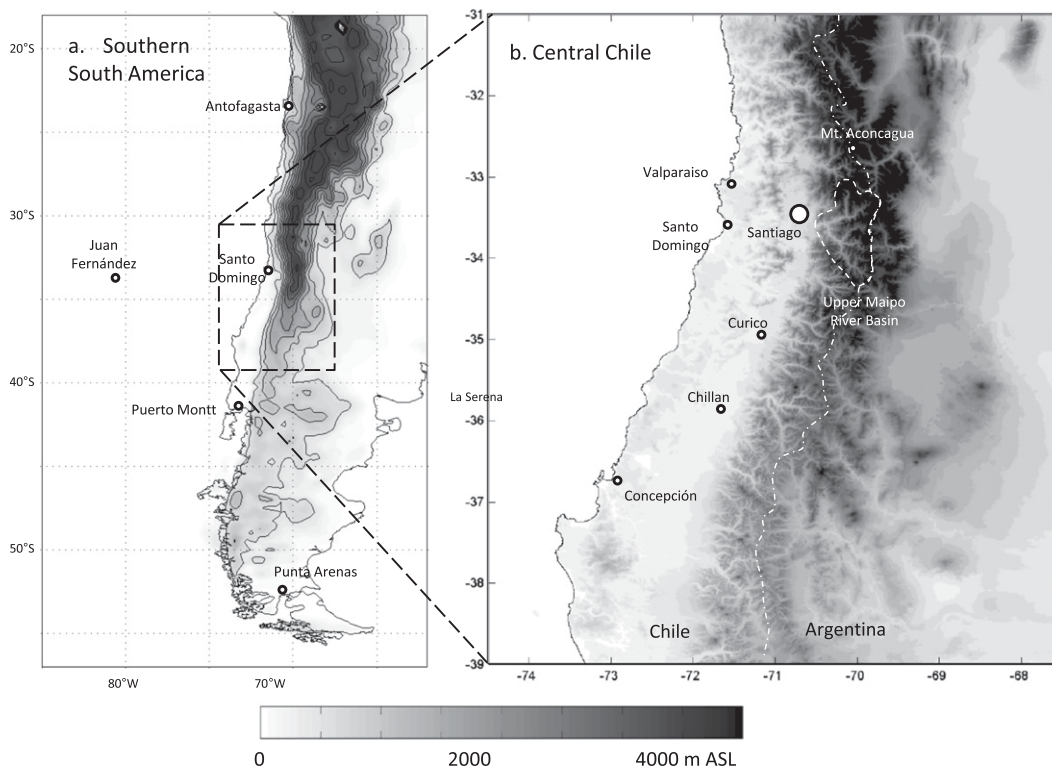


FIG. 1. Topographic maps of (a) southern South America showing the location of the four upper air stations operated by the DMC, and Juan Fernández Island, and (b) central Chile, showing several major cities (including Santiago), the Chile–Argentina border (coinciding with the Andean ridge), and the outlines of the upper Maipo River basin just east of Santiago.

Pacific moist air reservoir, feeding the precipitating clouds. In addition to these classical ingredients, the previous works have found an intense northerly low-level jet in the prefrontal sector extending eastward from the Andes to several hundreds of kilometers offshore (Barrett et al. 2009), apparently connected with upstream topographic blocking similar to what occurs along the western coast of North America (e.g., Neiman et al. 2004; Lundquist et al. 2010), leading to the formation of a barrier jet (Neiman et al. 2002, 2010).

The study of Viale and Nuñez (2011) further revealed that most of the heavy and extreme precipitation events in central Chile were associated with atmospheric rivers impinging on the subtropical Andes prior to the arrival of the cold front. The term atmospheric river refers to narrow (<1000 km) but elongated (>2000 km) corridors of intense water vapor transport in the lower troposphere, generally located in the broader warm and prefrontal zone of the polar front and particularly well defined over ocean areas (see Ralph and Dettinger 2011 for a review on atmospheric rivers). Since the seminal work by Zhu and Newell (1998), which coined the term and quantified their major contribution on the global poleward water vapor transport, the role of landfalling

atmospheric rivers in producing extreme rainfall events, major flooding, and heavy snowfall has been recognized in many midlatitude regions around the world (see Table 1).

By separating rainstorms according to the regional-mean accumulated precipitation, Viale and Nuñez (2011) and Barrett et al. (2009) showed that extreme events (e.g., more than  $40 \text{ mm day}^{-1}$  in Santiago) exhibit sharper and more intense features than ordinary events (e.g., a deep low off southern Chile). Falvey and Garreaud (2007) performed a more quantitative analysis by regressing a regional index of precipitation and selected profiles measured by the Santo Domingo radiosonde (coastal site at  $33^\circ\text{S}$ , the only upper-air station in central Chile), finding that the intensity of the low-level zonal flow (i.e., the flow against the mountains) accounts for  $\sim 40\%$  of the rainfall variance. The later value is comparable to its counterpart in mountainous coast of California, where Neiman et al. (2002) found that 55% of the variance of rainfall is accounted for wind variations based on hourly wind profile observations. Orographic enhancement by forced uplift (e.g., Roe 2005) is behind the strong relationship between low-level zonal flow and precipitation, a mechanism that seems to operate all along the

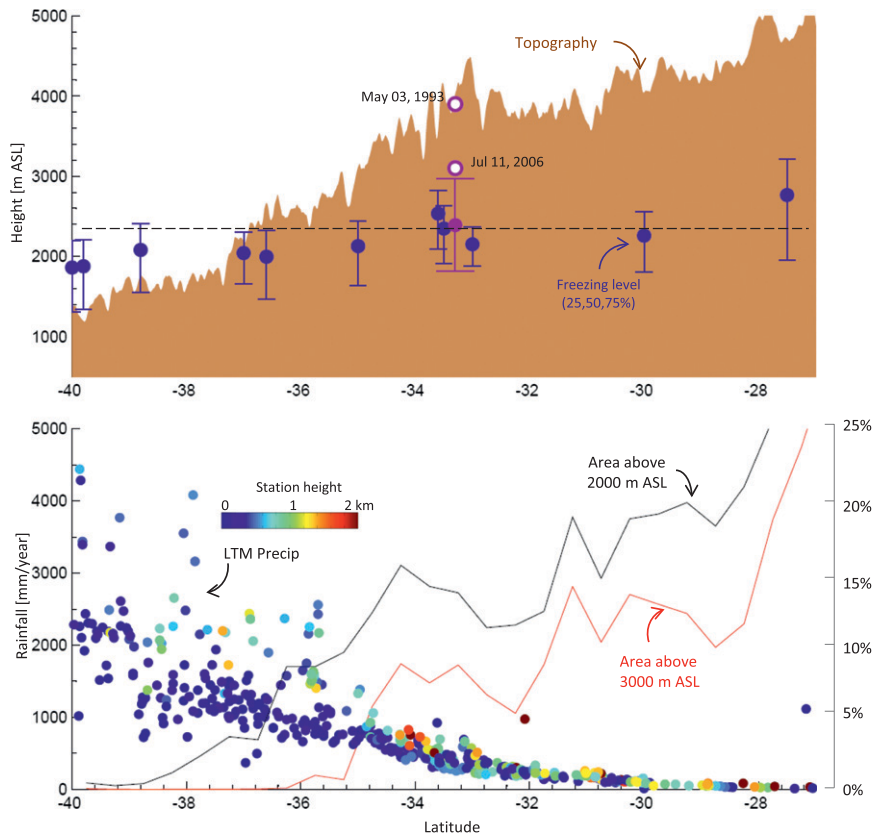


FIG. 2. Latitudinal variation of selected hydrometeorological parameters along central Chile. (top) Freezing level ( $H_0$ ), including median and interquartile range of its empirical distribution during rainy days based on Santo Domingo radiosonde data (purple error bars) and surface air temperature (blue error bars; see text). Also included are  $H_0$  values at Santo Domingo on 3 May 1993 (major landslides near Santiago) and 11 July 2006 (case study in this work), as well as the topographic profile of the Andes cordillera (97.5% value of the terrain height distribution at each latitude). (bottom) Annual mean rainfall (circles, colored according to the station height) and percent area above 2000 and 3000 m MSL to the west of the Andean crest calculated every  $0.5^\circ$  of latitude.

extratropical west coast of South America at daily and longer time scales (Garreaud 2007; Garreaud et al. 2013).

An aspect less explored in central Chile rainstorms is their thermal structure and evolution. The low-level air temperature during rain events is important because it sets the freezing level (i.e., the  $0^\circ$  isotherm height,  $H_0$ ), a close proxy of snowline height (e.g., Minder et al. 2011; White et al. 2010). An early study found that  $H_0$  in central Chile varies from 1500 to 3500 m MSL during rainy days, with a mean value of 2200 m MSL (Garreaud 1992). Since the subtropical Andes reach more than 5000 m MSL, the interstorm and intrastorm variations of  $H_0$  lead to major changes in the pluvial area, the terrain surface that receives rainfall, and thus in the hydrological response that ultimately dictates the occurrence of hazardous events over the mountains and downstream (Sepúlveda and Padilla 2008). As shown later, a rise of

700 m of  $H_0$  with respect to its mean value doubles the water volume available for runoff in the upper Maipo river basin, just south of Santiago. A dramatic example of this occurred in 3 May 1993, when a moderately precipitating ( $25 \text{ mm day}^{-1}$ ) but extremely warm ( $H_0 \approx 4000 \text{ m MSL}$ ) rainstorm triggered massive landslides and debris flow along the Andean foothills just east of Santiago, causing more than 80 fatalities (Garreaud and Rutllant 1996, and references therein). The connection between anomalous warm conditions (i.e., higher than average freezing level) and flooding has also been noted in western Washington by Neiman et al. (2008a, 2011) in the context of intense land falling atmospheric rivers events.

Given their relevance and their lack of scrutiny, here I characterize warm rainstorms in central Chile during wintertime, providing a statistical description of their

TABLE 1. Selected references on precipitation events related to atmospheric rivers around the world. A comprehensive list of references can be found at <http://www.esrl.noaa.gov/psd/atmivers>.

Location	References
Southeastern Mediterranean	Krichak et al. (2012)
United Kingdom	Lavers et al. (2011)
Central United States	Moore et al. (2012); Rutz and Steenburgh (2012)
West coast of North America	Neiman et al. (2008a,b, and references therein)
California, United States	Ralph et al. (2005, 2006, and references therein)
Western Washington, United States	Neiman et al. (2011)
Norwegian west coast	Stohl et al. (2008)
West coast of South America	Viale and Nuñez (2011); this study

occurrence and hydrological impacts as well as a synoptic analysis of their structure and evolution. One may speculate that warm rainfalls are just brief periods before an otherwise ordinary storm. It turns out that warm rainstorms are long-lasting events, characterized by, among other things, the presence of an atmospheric river embedded on a band of strong zonal flow reaching western South America. The local conditions and synoptic environment of the warm storms are also contrasted against their counterpart during the more frequent cold rainstorms in central Chile. Thus, my synoptic analysis may be relevant in an operational context as forecasters can use it as a template for early detection and prognosis.

The paper is organized as follows. Section 2 describes the different datasets used later. In section 3, I analyze the storm-to-storm variability in temperature and freezing level, estimating the hydrological impacts of the freezing-level variations in regions where it is relevant. Examination of half-hourly data allows a classification

of storms in warm and cold categories, whose local behavior is presented in section 4. Section 5 provides a synoptic analysis of the first two weeks of July 2006 when a cold, typical storm was followed by a warm case, emphasis being placed in the second event. In section 6, I employ a compositing analysis to generalize some of the results found in the case study. Section 7 contains the summary of findings, including a conceptual model of central Chile warm rainstorms.

## 2. Datasets

The freezing level in central Chile was estimated using vertical air temperature profiles (section 3) measured by radiosondes launched at Santo Domingo, a coastal station at 33°S, about 100 km west of Santiago (Table 2). The radiosondes at Santo Domingo are launched twice daily (1200 and 0000 UTC, or 0800 and 2000 LT) by the Chilean Weather Service (DMC) since September 1999. Prior to this date (1968–99), the launching location was at Quintero, also a coastal station, but about 80 km north of Santo Domingo. I also used the Santo Domingo radiosonde profiles of humidity, wind speed, and wind direction.

DMC also operates a network of surface stations at air terminals in Chile, from where I obtained daily accumulated rainfall (measured at 1200 UTC) and mean air temperature calculated as  $(T_{08} + T_{20} + T_x + T_n)/4$  for the winter months (April–September) from 1961 to 2011. I used 11 stations located between 28° and 40°S (Table 2), both at the coast and further inland, but all of them below 600 m MSL. DMC employs operational-grade instruments and applies stringent quality control to their data. Daily rainfall data were also available on a denser network over central Chile for my case study (July 2006) from simple, nonautomated gauges operated

TABLE 2. Meteorological station names, coordinates and variables:  $T$ , air temperature;  $R$ , rainfall;  $p$ , pressure; RH, relative humidity;  $V$ , wind.

Station name	Latitude	Longitude	Elevation (m)	Variables
Copiapo	27.2°S	70.3°W	291	Daily $T$ , $R$
La Serena	29.9°S	71.2°W	146	Daily $T$ , $R$
Valparaiso	33.0°S	71.6°W	41	Daily $T$ , $R$
Quinta Normal*	33.4°S	70.7°W	520	Daily $T$ , $R$
DGF*	33.4°S	70.7°W	535	30-min $T$ , $R$ , $p$ , RH
Juan Fernandez**	33.6°S	78.8°W	30	Daily $T$ , $R$
Santo Domingo (upper air)	33.7°S	71.6°W	75	12-h $T$ , $p$ , $V$ , RH
Curicó	35.0°S	71.2°W	225	Daily $T$ , $R$
Chillan	36.6°S	72.0°W	148	Daily $T$ , $R$
Concepción	36.8°S	73.1°W	48	Daily $T$ , $R$
Temuco	38.8°S	72.6°W	114	Daily $T$ , $R$
Valdivia	39.6°S	73.1°W	16	Daily $T$ , $R$
Osorno	40.1°S	73.0°W	90	Daily $T$ , $R$

\* Stations in Santiago.

\*\* Island 800 km off central Chile.

TABLE 3. Streamflow (hourly data) station names, rivers, coordinates, and basin area.

Station name	River	Latitude	Longitude	Elevation (m)	Basin area (km <sup>2</sup> )
Chacabuquito	Aconcagua	32.8°S	70.6°W	1030	836
Rinconada	Mapocho	33.5°S	70.9°W	420	3060
El Manzano	Maipo	33.6°S	70.4°W	950	4968
El Valle	Claro	34.7°S	70.9°W	476	530

by the National Water Agency (DGA). DGA also provides hourly streamflow in selected rivers in Chile, and here I used four stations near Santiago (Table 3) gauging unregulated basins. To obtain higher temporal resolution in the meteorological data, I used 30-min averages of air temperature and precipitation at station DGF in Santiago (Table 2) from 2004 to 2011. This is a standard tripod-mounted Campbell automatic weather station (CS500 air temperature sensor and TE525 mm rainfall sensor) located on the roof of a university building about 30 m above ground level.

To characterize the atmospheric circulation I have used the recently released Climate Forecast System Reanalysis (CFSR) fully described by Saha et al. (2010) and provided by the National Centers for Environmental Prediction (NCEP). As in other reanalyses [e.g., NCEP–National Center for Atmospheric Research (NCAR) and 40-yr European Centre for Medium-Range Weather Forecasts (ECMWF) Re-Analysis (ERA-40)], CFSR employs all available observations (surface and upper air) and satellite retrievals assimilated on a state-of-the-art numerical model to produce the best estimate of the three-dimensional state of the ocean–atmosphere system for the 31-yr period 1979–2009. The main novelties of CFSR are its much higher spatial resolution (T382 horizontal resolution,  $\sim 38$  km and 64 vertical sigma levels) and temporal resolution (hourly outputs). Furthermore, the atmospheric component of CFSR is fully

coupled with an ocean model and a two-layer sea ice model. In this work I used the 3D pressure level data, available every 6 h on a  $0.5^\circ \times 0.5^\circ$  latitude–longitude grid interpolated every 25 hPa in the vertical (from 1000 to 50 hPa), provided by the National Climatic Data Center throughout its National Operational Model Archive and Distribution System (NOMADS) data server. To complement my synoptic analysis I used several satellite datasets, as described in Table 4.

To identify atmospheric rivers in my case study and compositing analysis, here I used the relatively high-resolution CFSR data and follow the criteria established by Ralph et al. (2004) and Neiman et al. (2008b). Namely, narrow plumes of high moisture [vertically integrated precipitable water (IPW) in excess of 20 mm] that are more than 2000 km long and less than 1000 km wide are identified as atmospheric rivers. Since Ralph et al. (2004) and Neiman et al. (2008b) employed integrated water vapor (IWV) from the Special Sensor Microwave Imager (SSM/I; Hollinger et al. 1990), I used one week (6–12 July 2006) of concurrent SSM/I-IWV and CFSR-IPW data to verify their correspondence. Over the southeast Pacific ( $20^\circ$ – $70^\circ$ S,  $180^\circ$ – $70^\circ$ W), both variables exhibit a linear relationship with a correlation coefficient  $r = 0.78$ , a root-mean-square of 1.5 mm, and a bias of 1.7 mm. The use of CFSR data also allowed us to verify that atmospheric rivers identified on the basis of IPW alone also exhibited low-level wind speed stronger than  $12 \text{ m s}^{-1}$  and integrated horizontal water vapor transport in excess of  $200 \text{ kg m s}^{-1}$ .

### 3. Freezing-level variability and hydrological impacts

In midlatitude storms most of the hydrometeor production occurs in the upper part of the nimbostratus by water vapor deposition on ice crystal and aggregation (e.g., Houze 1993). Once the ice crystals fall below the  $0^\circ\text{C}$  isotherm, the melting process can take a few minutes,

TABLE 4. Main characteristics of satellite data employed in this work.

Retrieved variable	Spatial resolution	Temporal resolution	Instrument/product	Satellite(s)	Reference
Precipitable water*	$0.25^\circ \times 0.25^\circ$	Twice daily	SSM/I	Defense Meteorological Satellite Program (DMPS)	Wentz (1997)
Surface winds* (nominally at 10 m)	$0.25^\circ \times 0.25^\circ$	Twice daily	QuikScat	DMPS	Wentz et al. (2001)
TRMM-adjusted merged infrared precipitation**	$0.25^\circ \times 0.25^\circ$	3 hourly	TRMM 3B42	TRMM	Huffman et al. (2007)
Visible imagery	1 km at nadir	3 hourly	Imager, channel 1	<i>GOES-12</i>	
Infrared imagery	4 km at nadir	3 hourly	Imager, channel 4	<i>GOES-12</i>	

\* Available from <http://www.ssmi.com>.\*\* Available from <http://disc.sci.gsfc.nasa.gov>.

explaining the coexistence of rain and snow when surface air temperature is in the  $\pm 3^\circ\text{C}$  range and leading to a vertical offset of  $\sim(50\text{--}200)$  m between the freezing level ( $H_0$ ) and the snow line height (Garreaud 1992; White et al. 2010). Thus, vertical profiles of air temperature measured by radiosondes or remotely sensed can help in monitoring the snow line. Close to the mountains, however,  $H_0$  may be located a few hundred meters below its free tropospheric counterpart (Minder et al. 2011).

To obtain the empirical distribution of  $H_0$  in austral winter (May–September) when precipitation is present, I interpolated the height of the  $0^\circ\text{C}$  level from the radiosonde profiles at Santo Domingo from 1999 onward. Precipitation events are defined by daily precipitation  $\geq 5$  mm at Santiago (recall the general aridity of this region; average daily precipitation is 20 mm), and I simply averaged the 1200 and 0000 UTC radiosonde values of  $H_0$ . The distribution is near normal, with a mean value of 2200 m MSL and a standard deviation of  $\sim 250$  m. These values agree well with a previous estimation based on Quintero radiosonde data (the former radiosonde station in the coast of central Chile) for 1968–98 (Garreaud 1992) as well as with a more stringent analysis using only cases with rain at 1200 and 0000 UTC. To spatially extend my analysis I also used surface air temperature observations to estimate  $H_0$  at other latitudes. A persistent low-level temperature inversion over central Chile (Muñoz and Undurraga 2010) results in a moderate correlation between surface air temperature and lower-troposphere air temperature at a daily scale ( $r \approx 0.4$ ). During days with precipitation, however, the vertical temperature profile tends to follow a moist adiabat so that  $H_0$  can be approximated by  $H_s + T_m/\Gamma_s$ , where  $H_s$  is the station height,  $T_m$  is the mean daily temperature (in  $^\circ\text{C}$ ), and  $\Gamma_s \approx 6^\circ\text{C km}^{-1}$  is the moist adiabatic lapse rate. Granted, this procedure adds several sources of uncertainty to individual  $H_0$  estimates, but I am confident that the ground-based  $H_0$  distributions are statistically robust. Indeed, the ground-based  $H_0$  distribution around  $33^\circ\text{S}$  compares favorably<sup>1</sup> with its free tropospheric counterpart (see Fig. 2a).

A summary of the radiosonde- and surface-based empirical distributions of  $H_0$  during rainy events in central Chile is presented in Fig. 2a by the median value and interquartile range as a function of latitude. The median value slightly decreases from  $\sim 2500$  m MSL in

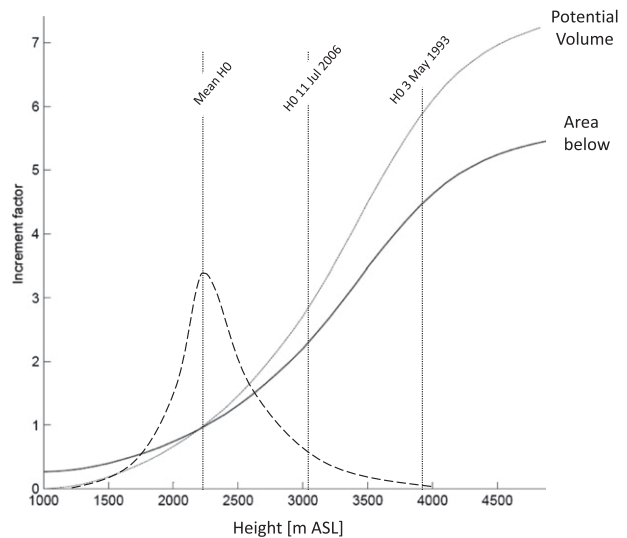


FIG. 3. Hypsometric curve (area below a given height) in the upper Maipo River basin defined by a control point at 1000 m MSL (just south of Santiago, see Fig. 1). The area has been normalized by the value at  $h = 2200$  m MSL, the median value of the freezing level ( $H_0$ ) over central Chile when precipitation is present. Also shown is the increment in available volume normalized by the value at  $h = 2200$  m MSL (see text), the fitted probability distribution of  $H_0$  (Gaussian curve), and the  $H_0$  values on 3 May 1993 and 11 July 2006 (vertical dashed lines).

the northern part to  $\sim 2000$  m MSL in the south. Nevertheless, the storm-to-storm variability is much higher than the median trend, and I conclude that freezing level (and snow line height) is rather uniform along central Chile. To put these numbers in context, Fig. 2a also shows the topographic profile of the Andes cordillera, which exhibits values well over 4000 m MSL to the north of Santiago but decreases southward down to 1000 m MSL at  $40^\circ\text{S}$ . Figure 2b also shows the fraction of area in central Chile above 2000 and 3000 m MSL, both of which rapidly decrease south of  $35^\circ\text{S}$ .

From Fig. 2 it is evident that  $H_0$  variability has little impact to the south of  $36^\circ\text{S}$ , where  $H_0$  is usually above the highest terrain so that ground precipitation is predominantly liquid. In the northern half of central Chile, however, changes in  $H_0$  produce significant changes in the pluvial area, the portion of the terrain receiving liquid precipitation. On the other hand, to the north of  $30^\circ\text{S}$  precipitation is very small, so the region between  $35^\circ$  and  $32^\circ\text{S}$  (including the Santiago area) is the most sensitive to  $H_0$  changes from a hydrological perspective.

Let us consider the upper Maipo River basin, which drains from the Andes toward the Pacific Ocean just south of Santiago. Figure 3 shows the area between 1000 m MSL and any given height, normalized by the area below 2200 m (the median value of  $H_0$  for central Chile). This graph also includes the  $H_0$  fitted distribution.

<sup>1</sup> Using a Student's  $t$  test and a Fisher test, I found that the mean value and standard deviation of  $H_0$  derived from the Santo Domingo radiosonde and Valparaiso ground data are not statistically different at the 2.5% confidence level.

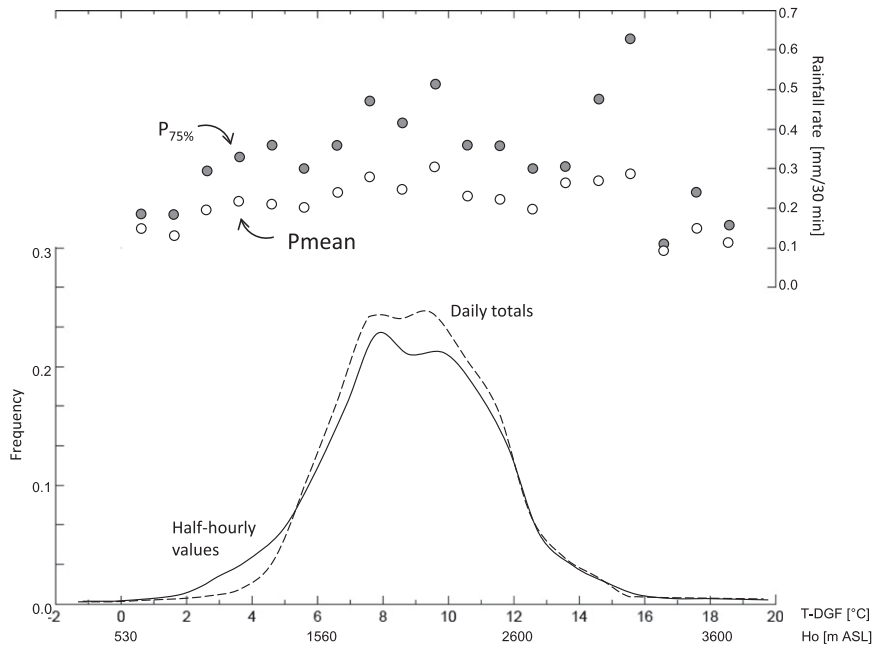


FIG. 4. Empirical probability distribution of the surface air temperature at DGF-Santiago (a proxy of the freezing level, see scale at the bottom) when precipitation is present using daily and half-hourly averages. Also indicated are the average and 75% quartile value of the half-hourly precipitation stratified according to air temperature in  $1^{\circ}\text{C}$  bins across the observed range.

If  $H_0$  rises to 3100 m (as in the case analyzed later), the pluvial area doubles with respect to the median case. Recall that above  $H_0$  precipitation accumulates as snow that will melt later, but below  $H_0$ , at least part of the rain will immediately become surface runoff, unless the previous snow line is too low. Similar area-increment factors are found for other Andean basins draining into central Chile.

Quantifying the actual increase in runoff given an increase in  $H_0$  is beyond the scope of this paper because it requires knowledge of the precipitation distribution with height and infiltration rates (both variable among storms). Let us offer here an estimate of the available volume for runoff simply calculated as the integral  $\int P(h) dA$  from the basin outlet (1000 m) to the level of  $H_0$ , where  $P(h)$  is the precipitation dependence with height. I assume a linear gradient of precipitation with height of  $+0.25 \text{ mm m}^{-1}$  taken from the climatological values presented in Falvey and Garreaud (2007). The increase in available volume as a function of height is also presented in Fig. 3 and is slightly more pronounced than the areal increment. If I consider now  $H_0 = 4000 \text{ m}$  MSL, the value for 3 May 1993, the volume increased by a factor of 5 with respect to a storm with the same precipitation but with  $H_0 = 2200 \text{ m}$ . This dramatic increase in the pluvial area was considered a trigger factor of the deadly landslides that affected the Andean foothills (between 800 and 1200 m MSL) of Santiago that day (Garreaud and Rutllant 1996).

#### 4. Warm and cold rainstorms

Daily mean temperature and daily accumulated rainfall are useful for a regional picture, but they blur their joint frequency distribution. To obtain a more detailed analysis, I now use half hourly records from station DGF in Santiago from 2004 to 2011 during austral winter (May–September). Figure 4 shows the empirical distribution of air temperature for rainy episodes using the 30-min records and the aggregated daily data [rainfall  $\geq 0.1 \text{ mm (30 min)}^{-1}$  or  $\geq 5 \text{ mm day}^{-1}$ , respectively]. Both distributions are near normal and their parameters do not differ statistically, lending support to the daily analysis presented in section 3. The half-hourly probability density function (PDF) is slightly displaced toward the cold side relative to the daily PDF, possibly because, in many cases, rainfall does not extend during the whole day. Figure 4 also shows the mean value and upper quartile of the rainfall distribution stratified in  $1^{\circ}\text{C}$  bins throughout the observed temperature range in Santiago ( $0^{\circ}$ – $20^{\circ}\text{C}$ ). The mean value exhibits little dependence with temperature, but relatively intense rainfall rates tend to occur under mild conditions ( $7^{\circ}$ – $10^{\circ}\text{C}$ ). There is also a peak in high rainfall rates during warm episodes ( $T > 12^{\circ}\text{C}$ ).

The question remains on whether the warm rainfall 30-min periods are isolated episodes or brief prefrontal conditions or whether they cluster into long-lasting events. To answer this I visually screened the rainfall

and air temperature time series at DGF-Santiago. A rainfall *event* was defined as a continuous period of rainfall during more than 6 h with accumulation exceeding 5 mm. This resulted in 73 events, 80% of them lasting between 12 and 36 h (caution was placed on not dividing a synoptic event in smaller events). A cursory analysis reveals a majority of cold, postfrontal cases but also a sizable number of events with warm conditions and little temperature change. Considering the unweighted time average of air temperature at DGF during the precipitation period (referred to as  $T|_P$ ), the events were divided into cold ( $T|_P \leq 9.5^\circ\text{C}$ , 60% of the events) and warm cases ( $T|_P \geq 10.5^\circ\text{C}$ , 30% of the events).

I then composited air temperature, surface pressure, and rainfall for the 24-h period before and after the precipitation onset ( $t_0$ ). To reduce dispersion and focus in their temporal evolution, both air temperature and surface pressure are relative to their value at  $t_0$  and precipitation was normalized by the event's total. The result is presented in Fig. 5b for each group. Air temperature during cold events exhibits a weak increase 12 h before the rain onset and a rapid, marked drop right at  $t_0$ , followed by cold conditions (typically in the  $3^\circ\text{--}8^\circ\text{C}$  range, mean  $T|_P = 7.2^\circ\text{C}$ ) that slightly recover afterward. The surface pressure reaches a minimum about 12 h before the rain onset followed by a rapid increase at the beginning of the event by 4 hPa on average. The rainfall has a clear peak within the first 6 h of the event. The surface temperature drop, increase in pressure, and highest rainfall rate at  $t_0$  are typical of a precipitation event caused by a cold front moving over subtropical latitudes (Seluchi et al. 2006).

Warm events, on the other hand, show very distinct features. Air temperature and surface pressure show little change before and during the rainfall period. Most cases, however, do show a small temperature drop and pressure rise toward the end of the event (24 h or more after  $t_0$ ), suggesting a delayed frontal passage. Likewise, rainfall is more uniformly distributed during the precipitation period. Average DGF-Santiago air temperature remains over  $10.5^\circ\text{C}$  during these warm events, with a mean value of  $T|_P = 12.2^\circ\text{C}$ , indicative of freezing level above 2700 m MSL well into the upper quartile of the  $H_0$  distribution. The combination of an extended (if not intense) rainfall period and moderately high air temperatures in these warm events set the stage for an enhanced hydrological response over central Chile, as described in section 3. It remains now to understand the synoptic environment of these events.

## 5. A case study

### a. Local conditions

To illustrate the regional conditions and synoptic-scale features of a warm storm, I analyzed a moderately

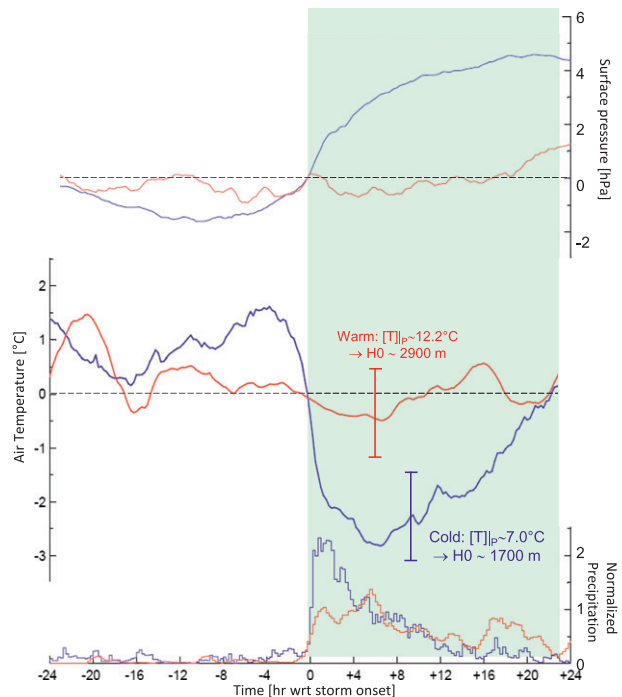


FIG. 5. Composite evolution of surface pressure, air temperature, and precipitation rate for the warm (red curves) and cold (blue curves) cases. Air temperature and pressure were normalized with respect to the value at the rainfall onset; precipitation was normalized with respect to event total accumulation. Error bars indicate the standard deviation within each group at selected times to illustrate dispersion among events.

rainy period on 11–12 July 2006. Figure 6 shows the local conditions at DGF-Santiago along with the vertical profiles of temperature and wind at Santo Domingo. Precipitation started around 0100 LT on 11 July and extended for the next 48 h, with a total accumulation of 49 mm. Air temperature was about  $11^\circ\text{C}$  the day before and slightly *increased* during the rainfall period, except at its end when it dropped about  $2^\circ\text{C}$  (but still remained over  $10^\circ\text{C}$  when rainfall was present). Likewise, surface pressure decreased during 11 July and recovered toward the final part of the event; rainfall rates were rather uniform throughout the event. In sum, the 11–12 July storm in Santiago featured the typical characteristics of a warm event noted in the previous section. In contrast, the precedent rainy period on 7–8 July (27 mm total) was classified as a cold case with temperature drop, pressure increase, and highest rainfall rates around the onset of the event. In the following, I focus in the warm event and contrast its features against the cold case.

The temperature profiles at Santo Domingo reveal a tropospheric-deep cooling from 4 to 8 July, particularly marked below 5000 m MSL (Fig. 6, middle). Consistently, the freezing level dropped from about 4500 m MSL in early July (dry period) to 1500 m MSL by 8 July when

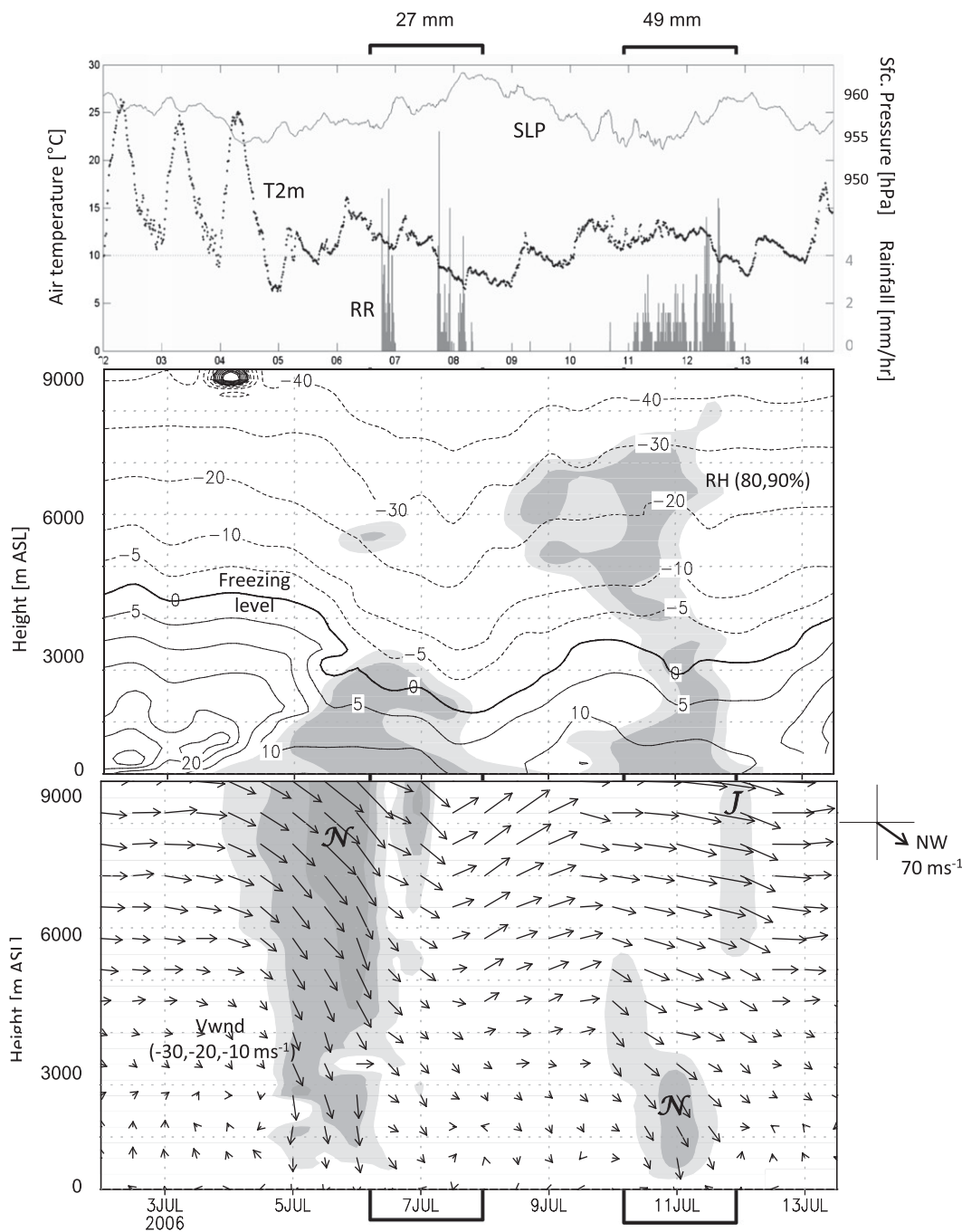


FIG. 6. (top) Time series of surface air temperature (dots), surface pressure (thin line), and rainfall rate (gray bars) at DGF-Santiago for 2 to 14 July 2006, when warm (11–12 July) and cold (7–8 July) rainstorms took place. Numbers at the top indicate accumulated rainfall in Santiago. (middle) Time–height diagram of the free tropospheric air temperature at Santo Domingo (contours every 5°C). The freezing level (the zero contour) is shown in bold. Dark (light) gray shading indicates relative humidity in excess of 90% (80%). (bottom) Time–height diagram of wind vectors at Santo Domingo. The *J* indicates maximum westerly flow in excess of 50 m s<sup>-1</sup>. The *N* indicates the maximum northerly flow. Gray shading indicates northerly winds in excess of -10 (light), -20 (medium), and -30 (dark) m s<sup>-1</sup>.

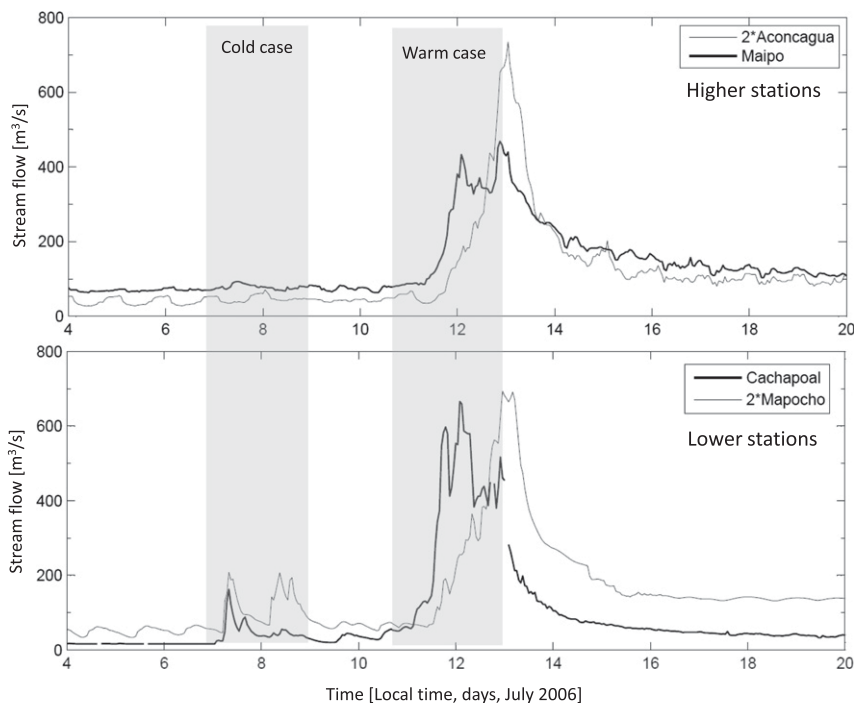


FIG. 7. Streamflow at four stations in central Chile during 4–20 July. (top) The higher stations ( $>900$  m) Aconcagua in Chacabuquito (thin line, streamflow  $\times 2$ ) and Maipo in El Manzano (thick line). (bottom) The lower stations ( $<500$  m) Mapocho in Rinconada (thin line, streamflow  $\times 2$ ) and Claro in El Valle (thick line). See Table 3 for station location and basin areas.

most of the precipitation occurred in the first event. The free troposphere warmed rapidly on 9–10 July, so that  $H_0$  rose above 3000 m MSL and remained high during the warm precipitation period. Such marked storm-to-storm difference in the freezing level contributed to a disparate surface hydrological response (also note the difference in accumulated precipitation). Daily stream flows measured at four sites in central Chile (Table 3) are presented in Fig. 7. During the first cold event, a rainfall-driven increase in streamflow was detected in the lower-elevation stations but not in the higher stations located only 500–600 m below  $H_0$  in this case. In contrast, the flood associated with the warm rainfall case is evident at all stations that recorded a peak flow about 4–5 times larger than the base flow.

The wind profiles at Santo Domingo were also distinct between the warm and cold rainfall periods (Fig. 6, bottom). The pre-rainfall conditions of the cold event featured strong ( $>30$   $\text{ms}^{-1}$ ) northwesterly flow in the upper- and middle-troposphere that changed to northerly below 3000 m MSL. During the rainfall period, the midlevel winds rapidly changed to southwesterly. From 9 July onward, mid- and upper-level winds become almost completely westerly, reaching a maximum on 11–12 July. Even though the wind also changed to northwesterly

below the Andean crest level, the zonal flow at 3000 m MSL in the warm event was nearly twice as large as in the previous cold case and much stronger than the climatology of rainy events in central Chile (Fig. 8).

The strong flow against the Andes was associated with the westerly jet aloft but also suggests a weak topographic blocking consistent with a conditionally unstable profile in this event (e.g., Pierrehumbert and Wyman 1985; Smith 2006). The 1–3-km average of the moist Brunt Väisälä frequency ( $N_m^2$ ) at 0000 UTC 12 July is  $-0.15$   $\text{s}^{-1}$  while  $N_m^2 \approx +0.1$   $\text{s}^{-1}$  in the rainy composite of Falvey and Garreaud (2007, see their Fig. 6). Both the warm temperatures and high humidity in a deep layer contributed to the conditionally unstable profile. On the other hand, the strong zonal moisture flux at midlevels undoubtedly contributed to the extended prefrontal rainfall event by producing topographically enhanced precipitation (e.g., Roe 2005). I discuss later the relative roles of the orographic and background precipitation in this case.

#### b. Synoptic environment

For an initial picture of the synoptic environment during the warm and cold cases, Fig. 9 shows the CFRSR 500-hPa wind vectors superimposed on the Geostationary Operational Environmental Satellite 12 (*GOES-12*)

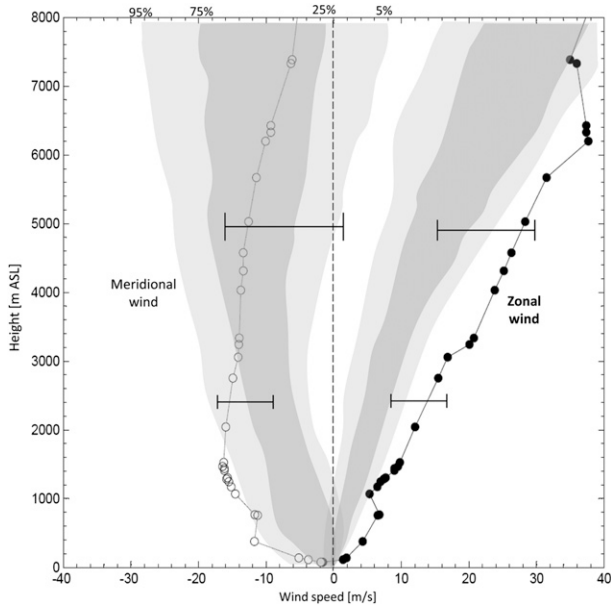


FIG. 8. Vertical profiles of the zonal (closed circles) and meridional (open circles) wind for Santo Domingo at 1200 UTC 11 Jul 2006. Also shown are the empirical distributions (shading for 5%, 25%, 75%, and 95% values) of the wind for days with precipitation in central Chile, regardless of the air temperature (adapted from Falvey and Garreaud 2007), as well as the interquartile range of the zonal and meridional components at 3 and 5 km during warm storms.

infrared (IR4) imagery at 1400 UTC 7 and 11 July 2006. The salient feature on 11 July was a nearly zonal band of high clouds at  $32^{\circ}$ – $35^{\circ}$ S over the Pacific that widens upon reaching the west coast of the continent. Collocated with the cloud band there were strong midlevel westerly winds. Farther south over the east Pacific there is a region of southerly flow that turns cyclonically over Patagonia, defining a trough limited to midlatitudes. In contrast, the midlevel trough on 7 July extended well into the subtropical Pacific ( $\sim 18^{\circ}$ S), producing the aforementioned northwesterly flow over central Chile. In this case, the high cloud deck was less extensive, but there is a clear hint of northwest–southeast–oriented cloud bands over the southeast Pacific in connection with the cold front (more evident in the visible channel, not shown).

A broader view of the atmospheric circulation reveals two key aspects of this warm event (Fig. 10). First, a band of high moisture air ( $IPW > 40$  mm) extended all the way from the tropical western Pacific to subtropical South America, along the equatorward side of an upper-level westerly jet. Most of the moisture was concentrated below the 850-hPa level in the form of an intense, well-defined atmospheric river (as per the identification criteria at the end of section 2). Examination of the IPW fields during the previous week (Fig. 11) shows a steady progress of the high water vapor corridor at subtropical

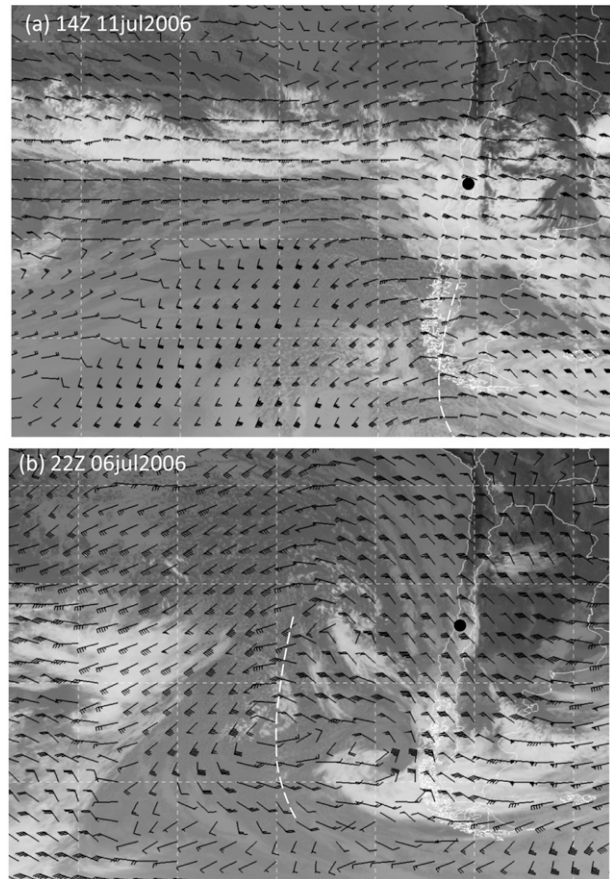


FIG. 9. GOES-12 IR4 imagery and 500-hPa CFSR wind over the southeast Pacific and southern South America at (a) 1400 UTC 7 Jul 2006 and (b) 2200 UTC 11 Jul 2006. White line indicates approximate position of the midlevel trough. The black circle indicates the location of Santiago in central Chile.

latitudes from the central Pacific ( $\sim 140^{\circ}$ W) to the Chilean coast with a phase speed of about  $7 \text{ m s}^{-1}$ . This atmospheric river originated in the western–central tropical Pacific moist reservoir, but it is well separated from the tropical east Pacific reservoir. The evolution of this atmospheric river across the Pacific as seen in the CFSR data is replicated in water vapor and rainfall satellite estimates [SSM/I–PW and Tropical Rainfall Measuring Mission (TRMM) not shown].

Second, heavily precipitating storms are often associated with a deep low off southern Chile (e.g., Viale and Nuñez 2011), but the surface analysis in Fig. 10 only exhibits a trough over Patagonia extending westward at  $38^{\circ}$ S and a closed low much farther east. Over the central Pacific, however, a strong anticyclone (central pressure  $> 1030$  hPa) is found at high latitudes that, in connection with the inverted omega pattern of the flow aloft, suggests a blocking situation. Indeed, a Hovmöller diagram of sea level pressure (SLP) along  $55^{\circ}$ S (Fig. 12) reveals

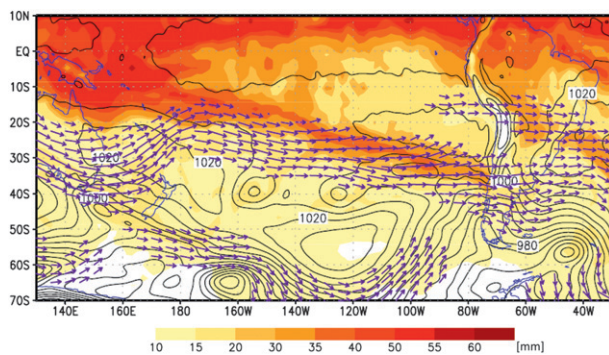


FIG. 10. Selected CFSR fields at 1800 UTC 11 Jul 2006 over the broad Pacific–South America region: IPW (shaded), 200-hPa wind (vectors, longest arrows at  $50 \text{ m s}^{-1}$ ), and SLP (contoured every 5 hPa).

the stagnation of this extratropical high over the South Pacific from 7 to 13 July. Similar evolution is seen at 500 hPa. The key role of the blocking high was the prolonged supply of cold air from higher latitudes around its eastern flank, enhancing the north–south temperature gradient that in turn maintained the zonal jet and, thus, the moisture transport, across the subtropical Pacific.

The relation between low-level circulation and precipitation is exposed in Fig. 13 using CFSR fields of accumulated precipitation and 950-hPa wind and temperature. Once again, I focus on the low-level evolution of the warm case (right column), but I also provide a description of the cold case (left column) to emphasize their differences. In the cold case, the cold front over the ocean is oriented from northwest to southeast, and it advances along the Chilean coast from  $38^\circ\text{S}$  to  $30^\circ\text{S}$  in less than 24 h, crossing over Santiago around 0000 UTC 8 July. Southerly winds over  $10 \text{ m s}^{-1}$  prevail in the postfrontal air mass. Precipitation occurs in a narrow band along the front that widens upon reaching the continent, with prefrontal precipitation restricted to the Andean ridge (a similar pattern is described in further detail in the study of Barrett et al. 2009). During the warm case, the cold front is more zonally oriented, with strong westerlies in the warm sector offshore and northwest closer to the coast because of the low-level mechanical blocking upstream of the Andes cordillera. Consistent with the weak southerlies in its cold sector ( $v \leq 5 \text{ m s}^{-1}$ ), the front advanced slowly northward, reaching  $\sim 32^\circ\text{S}$  toward the end of 12 July and causing the air temperature drop at DGF-Santiago noted before (Fig. 6, top). Precipitation fell on an ample prefrontal wedge over central Chile, with highest accumulation over the western slope of the Andes rapidly decreasing offshore. These CFSR precipitation features are in good agreement with surface observations and TRMM estimates (not shown). I attribute the slim

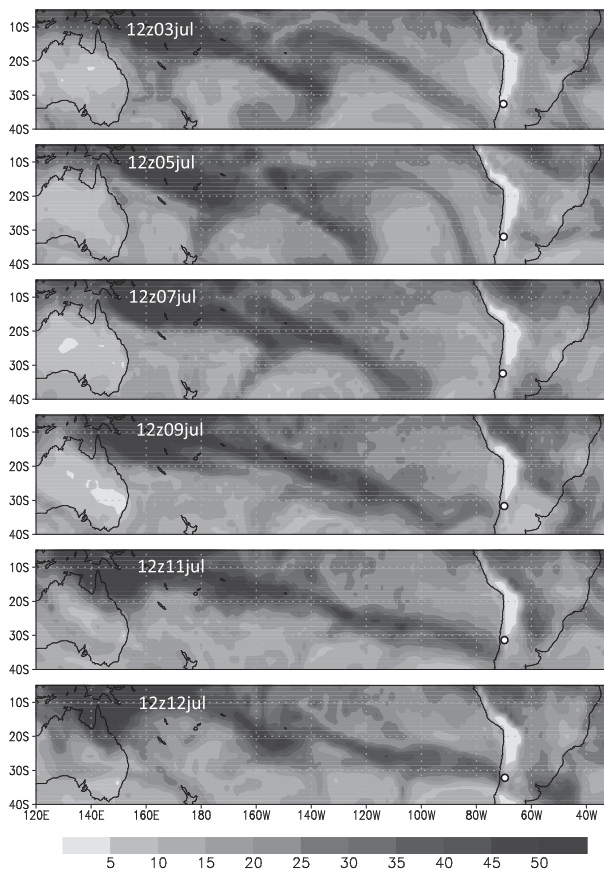


FIG. 11. (top to bottom) Time sequence of CFSR IPW (cm, shaded) over the Pacific–South America region at 1200 UTC from 3 to 12 Jul 2006 (every 2 days except for the last two). The white circle indicates the location of Santiago in central Chile.

background precipitation offshore to the weak low-level convergence over open ocean.

A pair of meridional and zonal cross sections (Fig. 14) helps to vertically expand my description, confirming the widespread cloud formation in the warm, moist sector ahead of the cold front, the intense westerlies impinging on the Andes of central Chile, and the deep area of upward motion upstream of the Andes. Thus, the larger precipitation inland, especially over the western slope of the Andes in central Chile, results from the localized uplift of the atmospheric river over the mountainous terrain within a warm, conditionally unstable air mass. This mechanism is similar to the cases described in California (Ralph et al. 2005; Smith et al. 2010) and over western Washington (Neiman et al. 2011) in connection with heavy rainfall and flooding events.

## 6. Large-scale composites

Let us now extend my compositing analysis to the large-scale circulation in order to generalize some of the

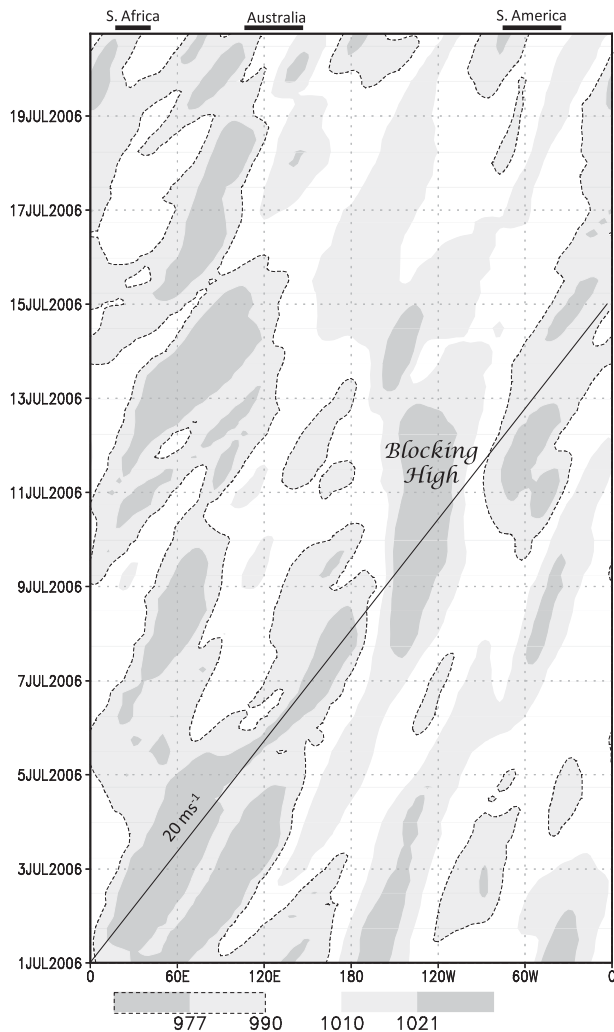


FIG. 12. Hovmöller diagram (time-longitude section) of SLP at 55°S constructed with 6-hourly CFSR analysis from 1–20 July 2006. Dashed lines enclosed values < 990 hPa. Note the quasi-stationary blocking high centered at 140°W from 7 to 13 July. Straight line indicates an eastward propagation of  $20 \text{ m s}^{-1}$ .

results obtained in my case study. To this effect I consider the same pool of warm (22) and cold (44) events selected in section 4 on the basis of the local conditions at DGF-Santiago and averaged selected fields at 0000, 0600, 1200, or 1800 UTC, whichever was closer to  $t_0$ . Figure 15 shows the composite vertically IPW and 200-hPa wind for each group. The cold composite (Fig. 15b) captures most of the features described in previous synoptic analysis of central Chile rainfall (e.g., Barrett et al. 2011). They include a well-defined midlevel trough extending well into the subtropics and with its axis off the west coast of South America causing midlevel northwesterly winds over central Chile, as well as a surface closed low off southern Chile or over the Drake passage. The cold composite field of IPW exhibits

a broad area of high moisture extending from the eastern tropical Pacific toward central Chile. Indeed, although a band of moist air just ahead of the cold front (i.e., embedded in the broad warm conveyor belt) was found in all individual cold cases, only half of those can be classified as atmospheric rivers, in agreement with the findings of Viale and Nuñez (2011).

The warm composite exhibits a zonal band of high moisture across the eastern Pacific that reaches South America at 30°–35°S (Fig. 15a). Even the mean composite IPW field marginally satisfies the criteria for an atmospheric river, and I verified the existence of such a feature off central Chile in 18 out of the 22 warm cases. The composite atmospheric river is located along the equatorward side of the upper-level zonal jet stream and is well separated from the tropical eastern Pacific moist air reservoir that often feeds winter storms in central Chile. Using the SLP field I also determine the position of a closed cyclone, if any, around southern South America. It turns out that more than half of the warm cases feature only a trough in this area, and if a cyclone is present it is often located over the South Atlantic. Therefore, the warm composite pattern is quite similar to the case study (cf. Fig. 12) in two key aspects: a zonal atmospheric river reaching central Chile under a westerly jet aloft and a lack of a deep cyclone off southern Chile. Also noteworthy in the warm composite is the jet exit region just to the west of the subtropical Andes and weak flow at midlatitudes around 120°W.

The composite anomalies (i.e., departures from the wintertime long-term mean) of 500-hPa air temperature and SLP are shown in Fig. 16. The wide area of weakly negative SLP anomalies over southern South America in the warm composite is consistent with the low density of cyclones commented before. Farther west over the South Pacific, there is an elongated band of positive SLP anomalies indicative of recurrent blocking episodes (or slowly moving anticyclones) in this group (Fig. 16a). In between the positive and negative centers ( $\sim 100^\circ\text{W}$ ) there is anomalous flow right from the south sustaining an area of cold midlevel temperature anomalies that extends zonally at 40°S. Farther north over the subtropical east Pacific there is also an area of intense warm anomalies whose origin remains unclear but may be associated with upper-level subsidence at the equatorward side of the jet stream exit (R. Rondanelli 2012, personal communication). In any case, the westerly jet aloft at subtropical latitudes is in thermal wind balance with this marked meridional temperature gradient. On the other hand, the cold composite (Fig. 16b) features a transient, baroclinic wave train with the midlevel thermal anomalies a quarter of the cycle out of phase with their SLP counterparts.

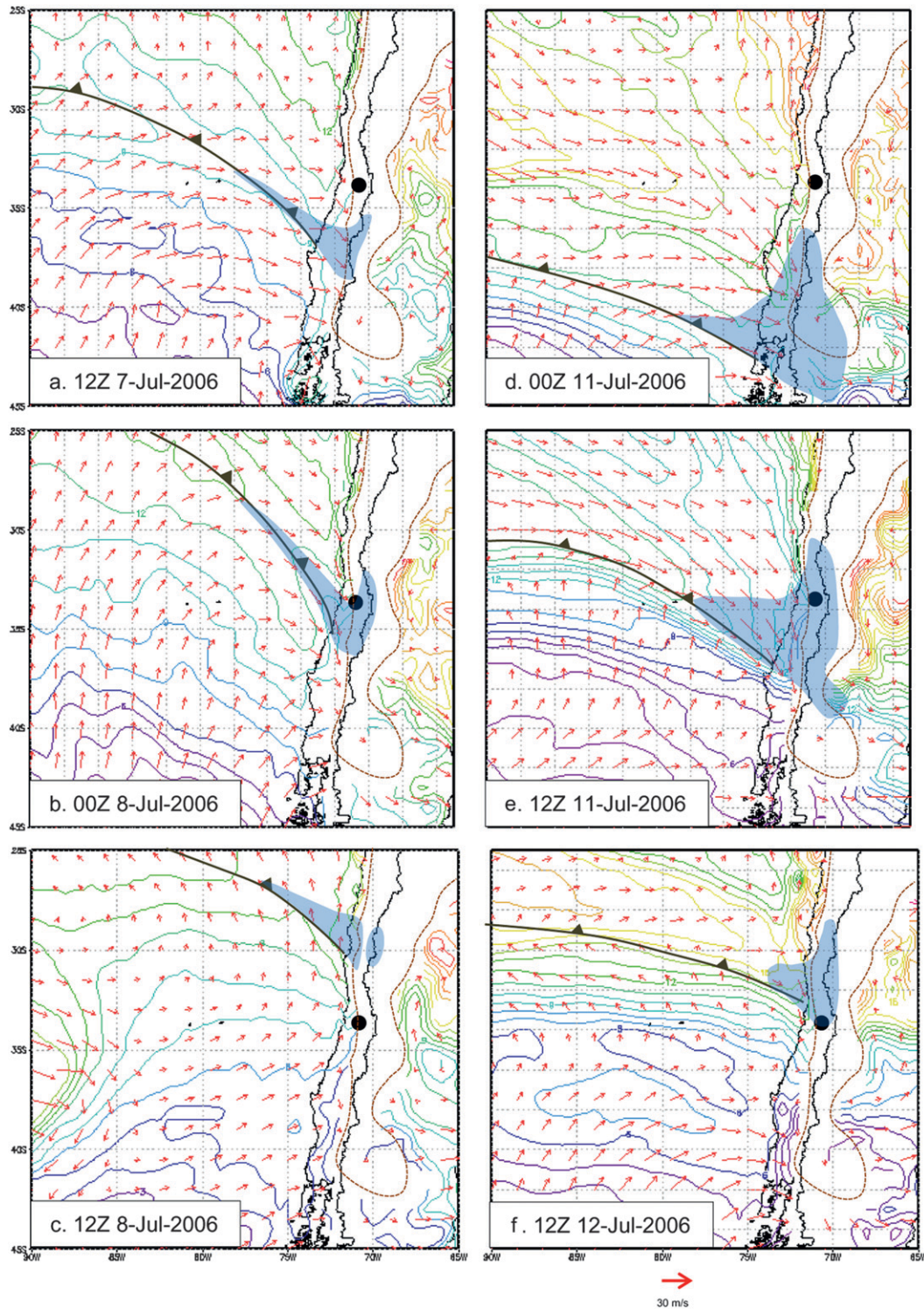


FIG. 13. CFSR air temperature (contoured every 1°C) and wind vectors (arrows) at 950 hPa for selected dates–times during (a)–(c) the cold event and (d)–(f) the warm event. Cold fronts are marked for each date–time using analysis of the temperature, wind, and pressure fields. Blue shading indicates 3-h accumulated precipitation > 2 mm. Terrain > 1000 m MSL is encircled by the dashed brown line. Black circle indicates location of Santiago, Chile.

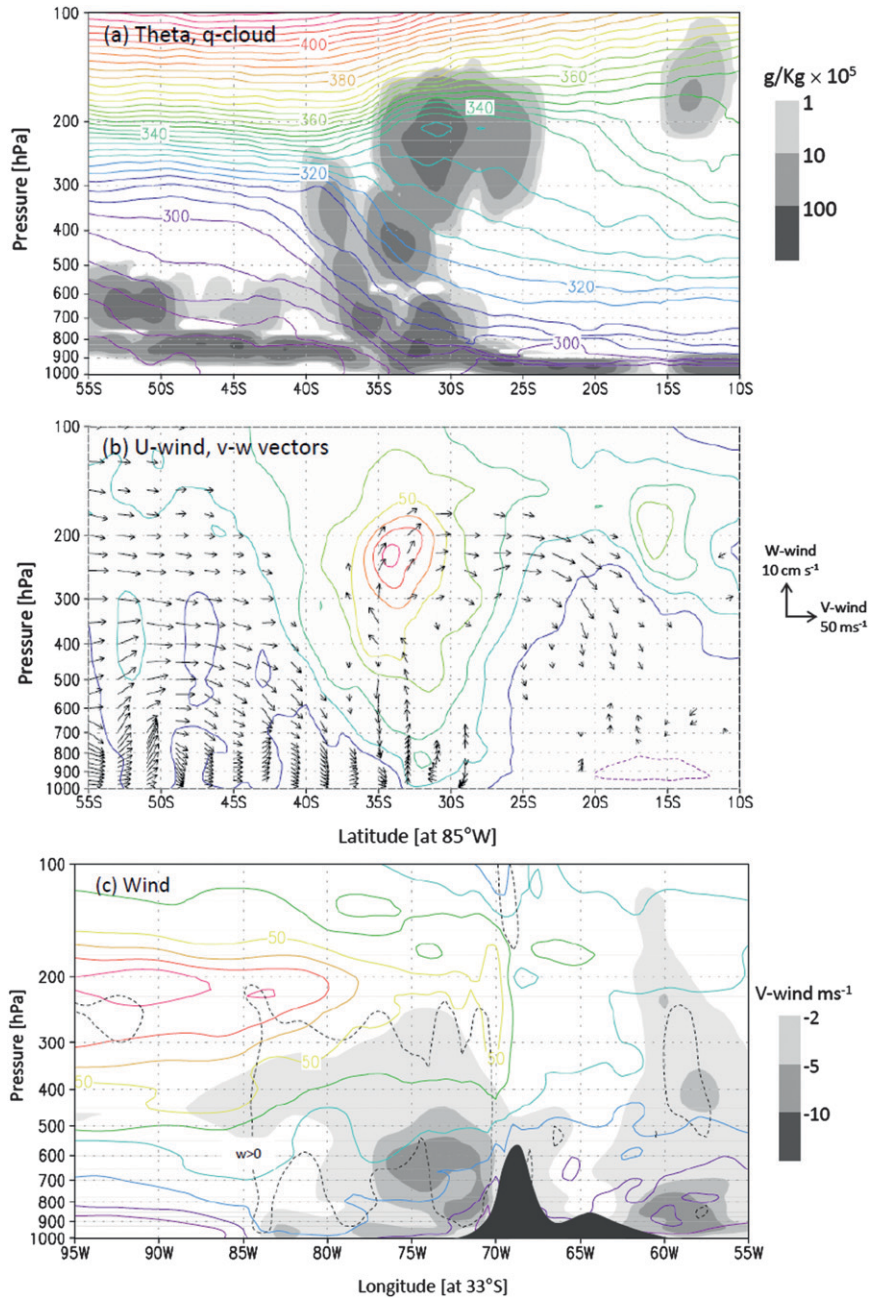


FIG. 14. Latitude–height cross sections of selected CFSR variables at 1800 UTC 11 Jul 2006 along 85°W (off the coast of Chile): (a) potential temperature (contoured every 5 K) and cloud mixing ratio (shaded) and (b) zonal wind component (contoured every 10 m s<sup>-1</sup>; the zero line is omitted, negative values in dashed lines) and (*v*, *w*) wind vectors. (c) Longitude–height cross section along 33°S at 1800 UTC 11 Jul 2006 of the zonal (colored contours every 10 m s<sup>-1</sup>) and meridional (shaded) wind components; dashed line encloses area of ascending motion.

I also used the radiosonde data at Santo Domingo (1200 UTC) to obtain the mean value of selected variables during wintertime warm storms and compare them with their background value for all winter rainstorms in central Chile (from Falvey and Garreaud 2007). Figure 8 illustrates the much stronger zonal wind component at

3000 m and 5000 m MSL in the warm composite. The mean meridional wind tends to be slightly stronger at lower levels (consistent with the stronger flow impinging the mountains) but rapidly decreases at higher levels. Likewise, the warm-composite, low-tropospheric moist Brunt Väisälä frequency results  $-0.1 \pm 0.1 \text{ s}^{-1}$ , revealing

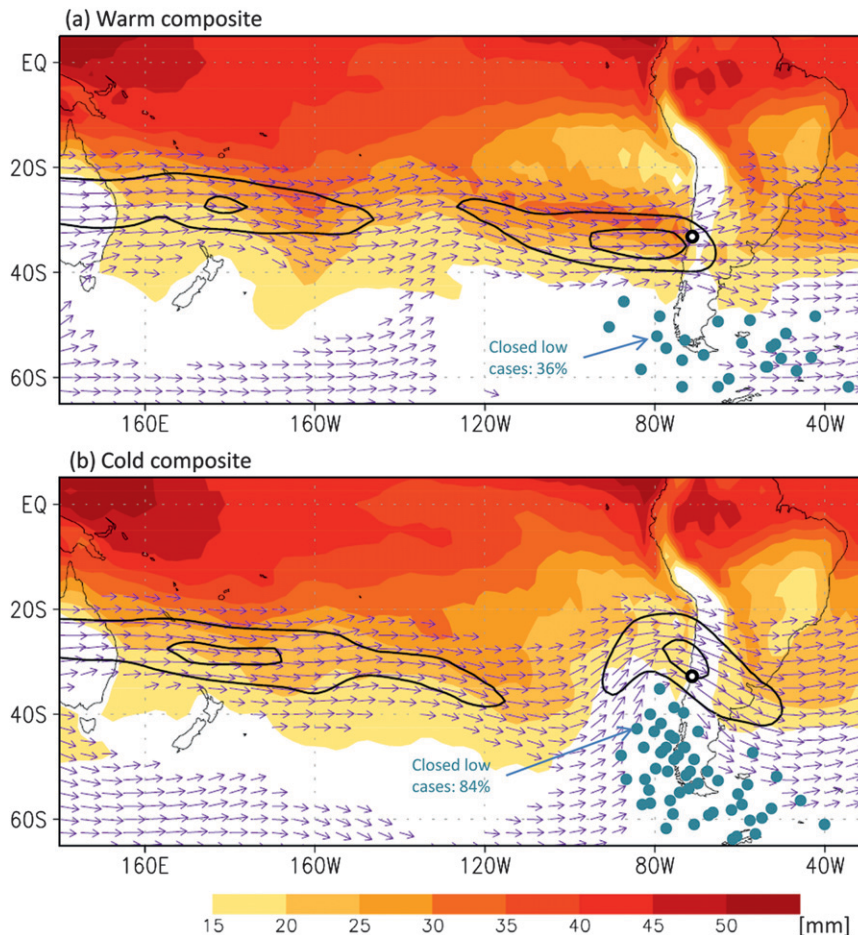


FIG. 15. Mean large-scale circulation for (a) 22 warm and (b) 44 cold rainstorms in central Chile. The composited CFSR fields are 200-hPa wind vectors and wind speed (contours are 30 and  $50 \text{ m s}^{-1}$ ) and integrated precipitable water (shaded). The black with enclosed white circle indicates the location of Santiago in central Chile. Visual inspection of the SLP field in each case allowed determination of the cyclone (if any) center positions, indicated by dark–light blue solid circles.

the recurrence of conditional instability during warm storms in contrast with more stable conditions in the majority of the cold cases. Furthermore, my warm composite wind, moisture, temperature, and stability profiles are similar to the mean profiles of the “mountain enhanced precipitation” group presented in Falvey and Garreaud (2007) on the basis of the events with much higher precipitation up in the Andes compared with stations at lower levels in central Chile (their Figs. 11 and 13). This is consistent with the prominent role of the orographic precipitation relative to the background (frontal) precipitation during warm rainstorms.

## 7. Conclusions

Using surface and upper-air observations, remote-sensed data, and high-resolution atmospheric reanalysis,

I have characterized winter storms in central Chile, with emphasis on their low-level thermal structure that is important for the surface hydrological response. I began by describing the frequency distribution of the freezing level ( $H_0$ ), a close proxy of the snowline separating rain and snow in the vertical. The median value of  $H_0$  (when precipitation is present) slightly decreases southward along the western slope of the Andes, from  $\sim 2300 \text{ m MSL}$  at  $25^\circ\text{S}$  to  $\sim 1900 \text{ m MSL}$  at  $40^\circ\text{S}$ . Interstorm  $H_0$  variability is large ( $\sigma \approx 250 \text{ m}$ ) and especially relevant between  $35^\circ$  and  $32^\circ\text{S}$  (including the Santiago metropolitan area), where Andean basins have their headwaters above  $5000 \text{ m MSL}$ . If I consider a basin outlet point at  $1000 \text{ m MSL}$ , an increase in  $H_0$  from  $2200$  (its mean value) to  $3200 \text{ m MSL}$  (80% percentile) leads to a twofold pluvial area increment and an even larger increase in the available rain volume, leading to possible

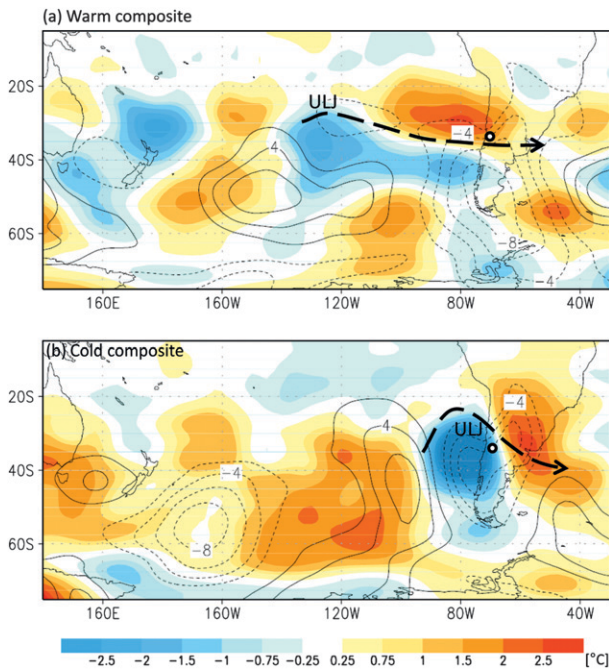


FIG. 16. Mean large-scale circulation for (a) 22 warm and (b) 44 cold rainstorms in central Chile. The composited CFSR fields are 500-hPa air temperature anomalies (shaded) and SLP anomalies (contoured every 2 hPa; the zero line is omitted, negative anomalies in dashed lines). The black with enclosed white circle indicates the location of Santiago in central Chile. The thick dashed line indicates the axis of the upper jet stream (from Fig. 15).

flooding, landslides, and debris flows along the Andean foothills if precipitation is high or prolonged.

Half-hourly meteorological records at DGF-Santiago allowed a detailed examination of local conditions during winter storms. As expected from previous studies and my synoptic experience, events often last 12–36 h and exhibit an air temperature drop ( $>3^{\circ}\text{C}$ ), a pressure increase ( $>4\text{ hPa}$ ), and the highest precipitation rates within the first hours of the rainfall onset. Indeed, about 60% of the cases scrutinized between 2004 and 2011 follow this behavior associated with the passage of a cold front over central Chile. After the initial drop, air temperature in Santiago remains below  $8^{\circ}\text{C}$  during the rainfall period, and the freezing level over central Chile is typically located between 1700 and 2300 m MSL. About 30% of the storms, however, exhibit warm near-surface air temperatures in central Chile ( $>11^{\circ}\text{C}$  at DGF-Santiago) and freezing levels in the upper quartile ( $H_0 > 2700\text{ m MSL}$ ) of the distribution. In these cases there is little temperature and pressure change, as well as rather uniform precipitation rates, throughout the rainfall period. Eventually, a cold front crossed the region, but a day or more after the rainfall onset.

The synoptic-scale environment during warm rainstorms was analyzed in detail for a typical case on 11–12 July 2006 and then generalized using a compositing analysis of 22 of such cases. The study case was contrasted with a precedent cold event on 7–8 July, and I also performed a compositing analysis of 44 cold cases. The main findings of these analyses—complemented by previous results on cold events—are shown schematically in Fig. 17. To guide this description let us consider two main questions: 1) what are the regional-scale conditions producing precipitation? and 2) how is the large-scale circulation pattern supporting these events?

Precipitation in the cold storms is concentrated along a cold front arching equatorward over the eastern Pacific, where intense low-level convergence takes place (Fig. 17a). An atmospheric river was found in more than half of the cases in this category, and their presence presumably dictates the rainfall intensity inland (Viale and Nuñez 2011). Closer to the coast, mechanical blocking upstream of the Andes results in a northerly, coast-parallel, low-level jet, further enhancing convergence in the near-shore region and causing a precipitation maximum (Barrett et al. 2009). Inland, precipitation is initiated over the sloping frontal surface, thus falling mostly over the cold air sector, although prefrontal precipitation may occur at higher elevations because of mechanical uplift of the midlevel, zonal flow over the western slope of the Andes (Falvey and Garreaud 2007). As per the large-scale circulation pattern, cold events feature a mid- and upper-level trough extending well into the subtropics and with its axis to the west of the continent so that strong northwesterlies prevail over central Chile. A closed low is often located off southern Chile, providing the dynamical forcing of the southerly winds in the cold, postfrontal sector.

During most part of a warm storm, precipitation over central Chile is not caused by convergence along a front (which is often weak and reaches the coast farther south) but rather by mechanical uplift of moist air over the western slope of the Andes (Fig. 17b). Indeed, atmospheric rivers were detected off central Chile in more than 80% of the warm cases, and even the mean composite field of IPW features an atmospheric river. Consistently, maximum precipitation occurs inland and presumably at mid-elevations, as reported by Falvey and Garreaud (2007) in their mountain-enhanced composite storms (see their Fig. 11). Furthermore, this mechanism is similar to the cases described in the Sierra Nevada (Smith et al. 2010) and over western Washington (Neiman et al. 2011) in connection with heavy rainfall and flooding events.

The dominant role of the orographic precipitation during warm storms stems from two ingredients. First, these cases are characterized by an intense, mostly zonal jet stream aloft right over central Chile and, hence, strong

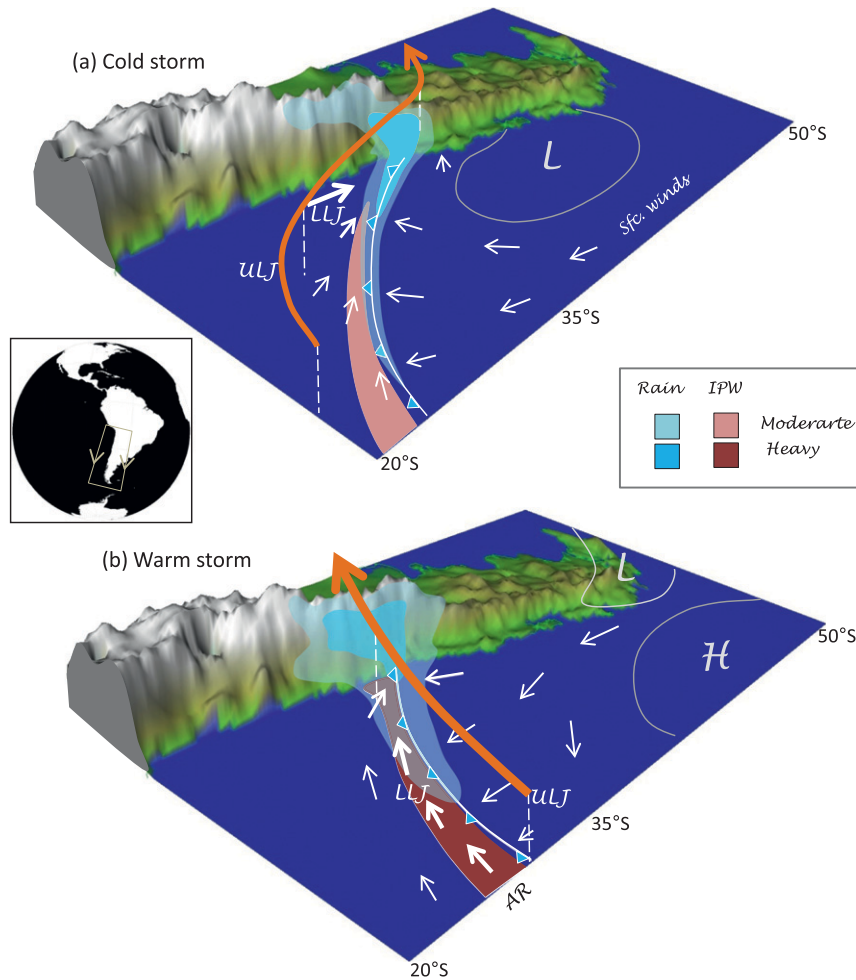


FIG. 17. Conceptual model of cold and warm rainstorms in central Chile superimposed on a 3D view from the northwest (see inset). In each case, the illustration shows the position of the cold front (conventional symbol), upper-level jet stream (orange arrow), low-level jet (thick white arrows), surface winds (thin white arrows), areas of moderate–heavy precipitation (blue shades), atmospheric rivers (moderate–heavy IPW, magenta shades), and pressure centers at midlatitudes (white contours).

winds impinging against the mountain range. Second, the moist, warm conditions that prevail in these events significantly reduce the mechanical blocking of the Andes leading to a broad layer of ascending motion just upstream of the mountains capable of drawing moist low-level air. The forced ascent can also release any potential instability present in the prefrontal air mass, as seems the case in the warm event on 3 May 1993 (Garreaud and Rutllant 1996).

The large-scale environment during warm storms often features just a trough around southern South America but a strong high farther to the west. As hinted in the composite (Fig. 15) and evident in the study case (Figs. 12, 14), the extratropical anticyclone remains nearly stationary for several days over the south–central Pacific, fostering

advection of cold air along its eastern flank that subsequently spreads westward around 40°S. The so-produced cold anomalies at midlatitudes result in a marked north–south thermal gradient at low and midlevels sustaining an intense, tropospheric deep zonal jet across the central–eastern Pacific. At low levels the strong, persistent westerlies create a nearly zonal atmospheric river (just to the north of the jet axis) extending across the subtropical Pacific to the subtropical west coast of South America. In the 11 July 2006 case (and in many others), the water vapor that ultimately precipitates over central Chile can be traced back to the central Pacific over the course of the previous week.

While in this work I have provided a description of the common features of warm rainstorms in central Chile

during wintertime, there are many issues that need to be explored in the future. These include analysis of the differences among storms and related hydrological responses and sensitivity of the accumulated rainfall and streamflow with respect to the atmospheric river position and orientation, as well as the predictability of these events. Given the connection of warm rainstorms and blocking conditions over the South Pacific, a phenomena with intraseasonal and interannual dependence, I also plan to address year-to-year changes of these storms as well as their occurrence under global warming scenarios.

*Acknowledgments.* I acknowledge FONDECYT Grant 1110169 and FONDAP Grant 1511009. I am grateful for constructive comments by Dr. Dave Rahn, Brad Barrett, Ricardo Muñoz, and two anonymous reviewers.

#### REFERENCES

- Barrett, B. S., R. D. Garreaud, and M. Falvey, 2009: Effect of the Andes Cordillera on precipitation from a midlatitude cold front. *Mon. Wea. Rev.*, **137**, 3092–3109.
- , D. B. Krieger, and C. P. Barlow, 2011: Multiday circulation and precipitation climatology during winter rain events of differing intensities in central Chile. *J. Hydrometeorol.*, **12**, 1071–1085.
- Catto, J., C. Jakob, G. Berry, and N. Nicholls, 2012: Relating global precipitation to atmospheric fronts. *Geophys. Res. Lett.*, **39**, L10805, doi:10.1029/2012GL051736.
- Cortés, G., X. Vargas, and J. McPhee, 2011: Climatic sensitivity of streamflow timing in the extratropical western Andes Cordillera. *J. Hydrol.*, **405**, 93–109.
- Falvey, M., and R. Garreaud, 2007: Wintertime precipitation episodes in central Chile: Associated meteorological conditions and orographic influences. *J. Hydrometeorol.*, **8**, 171–193.
- Garreaud, R., 1992: Estimación de la altura de la línea de nieve en cuencas de Chile central. *Rev. Chil. Ing. Hidraul.*, **7**, 21–32.
- , 2007: Precipitation and circulation covariability in the extratropics. *J. Climate*, **20**, 4789–4797.
- , and J. Rutllant, 1996: Análisis meteorológico del los aluviones de Antofagasta y Santiago de Chile en el periodo 1991–1993. *Atmosfera*, **9**, 251–271.
- , M. Vuille, R. Compagnucci, and J. Marengo, 2009: Present-day South American climate. *Palaeogeogr. Palaeoclimatol. Palaeoecol.*, **281**, 180–195.
- , P. Lopez, M. Minvielle, and M. Rojas, 2013: Large-scale control on the Patagonia climate. *J. Climate*, **26**, 215–230.
- Hollinger, J. P., J. L. Peirce, and G. A. Poe, 1990: SSM/I instrument evaluation. *IEEE Trans. Geosci. Remote Sens.*, **28**, 781–790.
- Hoskins, B. J., and K. I. Hodges, 2005: New perspectives on the Northern Hemisphere winter storm tracks. *J. Atmos. Sci.*, **59**, 1041–1061.
- Houze, R. A., Jr., 1993: *Cloud Dynamics*. International Geophysics Series, Vol. 53, Academic Press, 573 pp.
- Huffman, G. J., and Coauthors, 2007: The TRMM Multisatellite Precipitation Analysis: Quasi-global, multi-year, combined-sensor precipitation estimates at fine scale. *J. Hydrometeorol.*, **8**, 38–55.
- Krichak, S., J. Breitgand, and S. Feldstein, 2012: A conceptual model for the identification of active Red Sea trough synoptic events over the southeastern Mediterranean. *J. Appl. Meteor. Climatol.*, **51**, 962–971.
- Lavers, D. A., R. P. Allan, E. F. Wood, G. Villarini, D. J. Brayshaw, and A. J. Wade, 2011: Winter floods in Britain are connected to atmospheric rivers. *Geophys. Res. Lett.*, **38**, L23803, doi:10.1029/2011GL049783.
- Lundquist, J. D., J. R. Minder, P. J. Neiman, and E. Sukovich, 2010: Relationships between barrier jet heights, orographic precipitation gradients, and streamflow in the northern Sierra Nevada. *J. Hydrometeorol.*, **11**, 1141–1156.
- Minder, J. R., D. R. Durran, and G. H. Roe, 2011: Mesoscale controls on the mountainside snow line. *J. Atmos. Sci.*, **68**, 2107–2127.
- Montecinos, A., and P. Aceituno, 2003: Seasonality of the ENSO-related rainfall variability in central Chile and associated circulation anomalies. *J. Climate*, **16**, 281–296.
- Moore, B. J., P. J. Neiman, F. M. Ralph, and F. Barthold, 2012: Physical processes associated with heavy flooding rainfall in Nashville, Tennessee, and vicinity during 1–2 May 2010: The role of an atmospheric river and mesoscale convective systems. *Mon. Wea. Rev.*, **140**, 358–378.
- Muñoz, R. C., and A. A. Undurraga, 2010: Daytime mixed layer over the Santiago Basin: Description of two years of observations with a lidar ceilometer. *J. Appl. Meteor. Climatol.*, **49**, 1728–1741.
- Neiman, P. J., F. M. Ralph, A. B. White, D. E. Kingsmill, and P. O. G. Persson, 2002: The statistical relationship between upslope flow and rainfall in California's coastal mountains: Observations during CALJET. *Mon. Wea. Rev.*, **130**, 1468–1492.
- , F. Martin Ralph, P. O. G. Persson, A. B. White, D. P. Jorgensen, and D. E. Kingsmill, 2004: Modification of fronts and precipitation by coastal blocking during an intense landfalling winter storm in Southern California: Observations during CALJET. *Mon. Wea. Rev.*, **132**, 242–273.
- , F. M. Ralph, G. A. Wick, Y.-H. Kuo, T.-K. Wee, Z. Ma, G. H. Taylor, and M. D. Dettinger, 2008a: Diagnosis of an intense atmospheric river impacting the Pacific Northwest: Storm Summary and offshore vertical structure observed with COSMIC satellite retrievals. *Mon. Wea. Rev.*, **136**, 4398–4420.
- , —, —, J. Lundquist, and M. D. Dettinger, 2008b: Meteorological characteristics and overland precipitation impacts of atmospheric rivers affecting the West Coast of North America based on eight years of SSM/I satellite observations. *J. Hydrometeorol.*, **9**, 22–47.
- , E. M. Sukovich, F. M. Ralph, and M. Hughes, 2010: A seven-year wind profiler-based climatology of the windward barrier jet along California's northern Sierra Nevada. *Mon. Wea. Rev.*, **138**, 1206–1233.
- , L. J. Schick, F. M. Ralph, M. Hughes, and G. A. Wick, 2011: Flooding in western Washington: The connection to atmospheric rivers. *J. Hydrometeorol.*, **12**, 1337–1358.
- Pierrehumbert, R. T., and B. Wyman, 1985: Upstream effects of mesoscale mountains. *J. Atmos. Sci.*, **42**, 977–1003.
- Ralph, F. M., and M. D. Dettinger, 2011: Storms, floods and the science of atmospheric rivers. *Eos, Trans. Amer. Geophys. Union*, **92**, 265–266, doi:10.1029/2011EO320001.
- , P. J. Neiman, and G. A. Wick, 2004: Satellite and CALJET aircraft observations of atmospheric rivers over the eastern North Pacific Ocean during the winter of 1997/98. *Mon. Wea. Rev.*, **132**, 1721–1745.
- , —, and R. Rotunno, 2005: Dropsonde observations in low-level jets over the northeastern Pacific Ocean from CALJET-1998 and PACJET-2001: Mean vertical-profile and atmospheric-river characteristics. *Mon. Wea. Rev.*, **133**, 889–910.

- , —, G. A. Wick, S. I. Gutman, M. D. Dettinger, D. R. Cayan, and A. B. White, 2006: Flooding on California's Russian River: Role of atmospheric rivers. *Geophys. Res. Lett.*, **33**, L13801, doi:10.1029/2006GL026689.
- Roe, G. H., 2005: Orographic precipitation. *Annu. Rev. Earth Planet. Sci.*, **33**, 645–671.
- Rutz, J. J., and W. J. Steenburgh, 2012: Quantifying the role of atmospheric rivers in the interior western United States. *Atmos. Sci. Lett.*, **13**, 257–261, doi:10.1002/asl.392.
- Saha, S., and Coauthors, 2010: The NCEP climate forecast system reanalysis. *Bull. Amer. Meteor. Soc.*, **91**, 1015–1057.
- Seluchi, M. E., R. D. Garreaud, F. A. Norte, and A. C. Saulo, 2006: Influence of the subtropical Andes on baroclinic disturbances: A cold front case study. *Mon. Wea. Rev.*, **134**, 3317–3335.
- Sepúlveda, S. A., and C. Padilla, 2008: Rain-induced debris and mudflow triggering factors assessment in the Santiago cordilleran foothills, Central Chile. *Nat. Hazards*, **47**, 201–215.
- Smith, B. L., S. E. Yuter, P. J. Neiman, and D. E. Kingsmill, 2010: Water vapor fluxes and orographic precipitation over Northern California associated with a landfalling atmospheric river. *Mon. Wea. Rev.*, **138**, 74–100.
- Smith, R. B., 2006: Progress on the theory of orographic precipitation. *Tectonics, Climate, and Landscape Evolution: Geologic Society of America Special Paper 398*, S. D. Willet et al., Eds., Penrose Conference Series., Geologic Society of America, 1–16.
- Stohl, A., C. Forster, and H. Sodemann, 2008: Remote sources of water vapor forming precipitation on the Norwegian west coast at 60° N—A tale of hurricanes and an atmospheric river. *J. Geophys. Res.*, **113**, D05102, doi:10.1029/2007JD009006.
- Viale, M., and M. N. Nuñez, 2011: Climatology of winter orographic precipitation over the subtropical central andes and associated synoptic and regional characteristics. *J. Hydrometeorol.*, **12**, 481–507.
- Wentz, F. J., 1997: A well-calibrated ocean algorithm for SSM/I. *J. Geophys. Res.*, **102** (C4), 8703–8718.
- , D. K. Smith, C. A. Mears, and C. L. Gentemann, 2001: Advanced algorithms for QuikScat and SeaWinds/AMSR. *Proc. IEEE 2001 International Geoscience and Remote Sensing Symposium 2001, IGARSS'01*, Sydney, NSW, Australia, IEEE, 1079–1081.
- White, A. B., D. J. Gottas, A. F. Henkel, P. J. Neiman, F. M. Ralph, and S. I. Gutman, 2010: Developing a performance measure for snow-level forecasts. *J. Hydrometeorol.*, **11**, 739–753.
- Zhu, Y., and R. E. Newell, 1998: A proposed algorithm for moisture fluxes from atmospheric rivers. *Mon. Wea. Rev.*, **126**, 725–735.